Journal of Electronics and Electrical Engineering
https://ojs.wiserpub.com/index.php/JEEE

Research Article

Robust Nonlinear Control for Synchronising and Regulating Neural Activity

Sebastián Martínez[1,2], Ricardo S. Sánchez-Peña[1,2], Demián García-Violini[2,3]

[1] Depto. de Investigación y Doctorado, Instituto Tecnológico de Buenos Aires (ITBA), Buenos Aires, Argentina
[2] Consejo Nacional de Investigaciones Científicas y Técnicas (CONICET), Buenos Aires, Argentina
[3] Depto. de Ciencia y Tecnología, Universidad Nacional de Quilmes, Quilmes, Buenos Aires, Argentina
E-mail: semartinez@itba.edu.ar

Received: 8 October 2024; **Revised:** 11 December 2024; **Accepted:** 24 December 2024

Abstract: Modulating neural activity in a systematic manner holds significant potential for advancing the understanding of brain functions and improving therapeutic strategies. To forecast the dynamics behind several brain activities, numerous neurobiological models have been developed, targeting both individual neurons and entire neural populations. In this context, control systems emerge as powerful tools for effectively linking inputs, such as neural stimuli, to measurable outputs. This study introduces a control framework aimed at regulating neural-mass activity, which has promising applications in pattern tracking, including rhythm generation and phase synchronisation. Given the strong connection of these mechanisms to real brain computations, the presented approach offers biologically relevant insights. To demonstrate this, the Wilson-Cowan model is used, in which stimuli are delivered via light signals to genetically engineered neurons expressing light-sensitive actuators. This proof of concept provides a foundation for future experimental applications in neurobiological systems control. Furthermore, building on previous results, this work integrates opsin dynamics, of the channelrhodopsin and halorhodopsin-type, to accurately model the optogenetic activation channels, enhancing the description of the actuation process.

***Keywords*:** Wilson-Cowan model, robust control, closed loop, optogenetics, opsin models, bio-engineering, brain rhythm, pattern tracking

1. Introduction

The field of closed-loop neuroscience has experienced rapid development, driven not only by technological advancements but also by its potential to significantly enhance causal investigation of neural processes and circuits, as well as its promise for developing effective treatments for neurological disorders and diseases. In recent years, this progress has occurred "*hand-in-hand*" with advances in brain imaging technologies [1], allowing real-time monitoring of neural activity (sensing), and optogenetic techniques [2], which enable precise physiological modulation of targeted variables (actuation). A significant portion of existing work in this area has been conducted empirically, based on detailed observations aimed at achieving neural modulation. For instance, deep brain stimulation (DBS) protocols often rely on trial-and-error methods [3]. Within this context, control system theory offers a systematic framework for the analysis and design of closed-loop modulation schemes, providing a suite of powerful tools that have proven effective in different fields,

DOI: https://doi.org/10.37256/jeee.4120255834

ranging from industrial processes to, for example, medical applications. To diversify the application of modelling and control in bioengineering, the readers can find different applications in, for example, [4, 5].

Considering complex neurobiological systems as dynamical structures, with underlying inputs and outputs, enable a structured way to approach various modulation and tracking goals through control strategies [6]. Many of these strategies fall under the category of model-based control, where the dynamic behaviour of the system is predicted in real-time using a suitable model, allowing the controller to generate an adequate control actuation, accordingly.

A broad range of models are available within the literature [6], covering from highly detailed biological representations, focusing on ionic current dynamics and/or synaptic connectivity, to more simplified but biologically plausible approximations. The choice of model depends on factors such as the neural circuit under investigation, the desired level of detail, computational constraints, and whether the model needs to run in real-time. Notably, for modelling neural populations, simplified models can be computationally efficient while still capturing critical phenomena, making them ideal for control applications. These models, commonly referred to as neural-mass models [7], describe the collective dynamics of groups of neurons, often characterised by average measurements such as firing rates or voltages. This approach, which lumps the behaviour of many individual neurons into an ensemble average, is a mean-field technique, akin to the representation provided by local field potentials (LFPs). For a detailed discussion on dynamical models in neurophysiology, particularly from a control perspective, the interested reader is referred to [6].

Among the most considered neural-mass models throughout the literature, the Wilson-Cowan (W-C) model is used to design and assess a control strategy [8, 9]. These authors introduced a mean-field framework for neural activity, which models the dynamics of spatially localised excitatory and inhibitory populations through coupled nonlinear differential equations The assumption that cells within these populations exhibit similar properties and responses is supported by the redundancy of processes and the dense interconnections among them, enabling a low-dimensional description. By focusing on a space-clamped version of the W-C model, spatial gradients can be ignored, simplifying the analysis. Thus, with this model the activity of each subpopulation decays exponentially, governed by a time constant that reflects the propagation of postsynaptic potentials. The nonlinear input term defines the proportion of cells in each subpopulation that responds to the given excitation level. This seminal approach was further explored and more specialised models were developed since its introduction. For instance, the works in [10], specifically for epilepsy modeling, and [11] used in the study of cortical projections in sensory signaling, are notable examples.

Incorporating actuation channels within neural-mass models is crucial to accurately modify the dynamics of closed-loop neural systems. Actuation mechanisms, such as optogenetics, allow precise manipulation of neural activity, offering high spatial and temporal resolution that enhances control over other neural modulation techniques [12, 13]. Neglecting these actuation dynamics can lead to oversimplified representations that fail to capture the full behaviour of the system, especially in real-time applications such as closed-loop control. In particular, optogenetics stands out as one of the most advanced techniques in neurophysiology, as it targets distinct cells based on type and/or functionality [14]. This is achieved through the use of opsins such as Channelrhodopsin (ChR), for excitatory drive (depolarisation), and Natronomonas pharaonis halorhodopsin (NpHR), for inhibitory drive (hyperpolarisation), enabling bidirectional manipulation of neural circuits. In particular, ChR (and its faster variants, such as Chronos and ChroME [15]) has been designed to optimise expression and function in mammalian systems, allowing for prolonged stimulation with improved photocurrents, while NpHR (and further engineered variants, e.g., eNpHR3.0 [16]) offers stable hyperpolarising currents with reduced desensitisation, crucial for bidirectional control of neural activity [17, 18]. For further application of control methodologies in neurophysiology, the interested reader in referred to [19, 20, 21].

Within this context, optogenetics, combined with a neural-mass model, can be used as the actuation channel, providing the capability to target specific neural populations with high accuracy. Without integrating a neural-mass model with an adequate actuation channel, a control model could overlook key variables such as the latency, duration, and intensity of neural responses, leading to ineffective modulation strategies.

In this study, a closed-loop control strategy is employed to induce specific brain rhythms in a synchronised manner. The W-C model is coupled with simplified dynamic models for excitatory and inhibitory opsins, of the channelrhodopsin and halorhodopsin -type, as proposed in [14]. A nonlinear control solution is proposed and implemented using an extended Kalman filter (EKF) to estimate the system state [22], required by the nonlinear control algorithm. Several brain rhythms

are induced using experimentally acquired LFPs from the mice motor cortex as reference signals [23]. Both a dual bidirectional-opsin scenario, utilising excitatory and inhibitory opsins, and a dual depolarising-opsin scenario, where only excitatory opsins (ChR-type) are employed, are assessed to compare their effectiveness. The tracking error is evaluated under a wide range of variations in both amplitude and frequency of artificial reference signals to assess the robustness of the control strategy. While other synchronisation types, such as oscillator coupling or frequency-amplitude interactions, have been explored in previous studies [24, 25], this approach integrates a more realistic experimental setup as a preliminary step toward real-world closed-loop neurophysiology applications. This work builds upon the findings of [26], with the key distinction that the present study incorporates opsin dynamics handled via feedforward control, which were not accounted for in the previous work. In addition, the results explicitly demonstrate the limitations and performance degradation when the system is actuated using only excitatory opsins, highlighting the importance of accounting for both excitatory and inhibitory channels in such a control framework.

The proposed control framework addresses a unique challenge in neurophysiological systems by transforming the underlying model to facilitate the application of model-based control techniques. Unlike general control applications, the neurophysiological model considered here lacks key properties, such as affine control structures, required for methods like sliding mode or feedback linearisation [27, 28, 29]. Therefore, a direct comparison with conventional control methods is not applicable. Instead, this study focuses on demonstrating the efficacy of our controller in the specific neurophysiological context, highlighting the advantages of our approach in this domain.

To sum up, this study presents a neuromodulation approach with the following key contributions:

- **Closed-Loop Control Framework**: A novel robust closed-loop control approach is developed by integrating the W-C model with optogenetic actuation dynamics, providing a structured methodology for neural activity modulation.
- **State Estimation**: The implementation of an EKF enables accurate state estimation from indirect measurements, such as local field potentials (LFPs), demonstrating that these are sufficient for decoding internal neural states.
- **Dual-Opsin Control Framework**: By utilising both excitatory (ChR) and inhibitory (NpHR) opsins, the research highlights a precise method for inducing specific brain rhythms tailored to real neural activity data.
- **Comparative Analysis**: Through illustrative examples, the performance of dual-opsin control is contrasted with single-opsin scenarios, revealing notable differences in tracking accuracy and overall efficacy.

The remainder of this paper is outlined as follows. Section 2 presents the selected dynamical model, introduces the considered opsin dynamics, and emphasises the key biological assumptions. In Section 3, the system architecture is detailed, along with an explanation of the proposed control strategy. Section 4 describes and simulates a specific case study based on experimental data and a defined control methodology. Lastly, Section 5 provides a discussion of the conclusions drawn from this research, with an eye toward future experimental implementation.

2. Biological and modelling background

2.1 *The Wilson-Cowan model*

In most neural-mass models, the dynamics of the system are represented by nonlinear differential equations that describe its state variables, which can be derived from physical interactions. Commonly selected variables include population activities or rates, which reflect the number of active neurons per unit time within a defined volume of tissue. The synaptic inputs to individual neurons within the network are treated as the system internal couplings. Additionally, a nonlinear mapping captures the input-output relationship for each neural population, analogous to the frequency-current curve (gain function) observed in single neurons [30]. The mean-field theory for neural activity is proposed by Wilson and Cowan [8], who derived coupled nonlinear differential equations for excitatory and inhibitory sub-populations localised in space. The model is a coarse-grained description of network dynamics aim to bridge the gap between theoretical and practical neuroscience, inspired by computational observations. This approach is based on the premise that local neurons

exhibit similar properties and responses due to their interconnectedness and redundancy in processing. Consequently, the space-clamped W-C model, which does not account for spatial gradients, can be expressed as follows:

$$\begin{cases} \tau_E \dot{E} &= -E + (1 - rp_{EE}) f_E(w_{EE}E - w_{EI}I + P), \\ \tau_I \dot{I} &= -I + (1 - rp_{II}) f_I(w_{IE}E - w_{II}I + Q). \end{cases} \tag{1}$$

The activity of each subpopulation exhibits exponential decay characterised by a time constant τ_i, where $i \in \{E, I\}$, which is linked to the spread of postsynaptic potentials. The input term with nonlinear weighting represents the fraction of cells in each subpopulation that respond to the excitation level indicated in the function argument. This formulation illustrates the functional coupling, both in feedback (within each subpopulation) and feedforward (between different subpopulations), weighted by positive constants w_{ij} (where $i, j \in \{E, I\}$), accounting for the average number of synapses per neuron. In general, each subpopulation is influenced by inputs from the others, which drive the changes in activity rates $\dot{E}$ and $\dot{I}$. The response function $f_i(\cdot)$ is generally sigmoidal, indicating that cell activation increases monotonically with adequate stimulus strength. The factors $(1 - rp_{ii})$, where $i \in \{E, I\}$, reflect the proportion of cells capable of firing, accounting for the spiking refractory period, while P and Q represent external current-like inputs. A schematic of the W-C model is depicted in Figure 1.

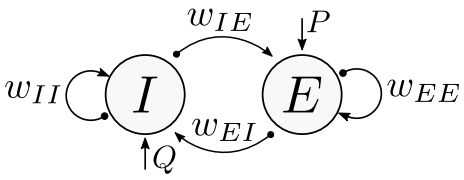

Figure 1. Schematic of the Wilson—Cowan model.

These inputs, P and Q, can be tailored for optogenetic control, incorporating both excitatory and inhibitory opsins (Opsins are light-activated ion channels [12] that can be engineered into the neuronal membrane).

Furthermore, the dynamics articulated in this framework are closely related to LFPs, which can be interpreted as a scaled representation of population spike rates (neural population activity). This connection highlights how the collective activity of neuron populations, modulated by, for example, optogenetic inputs combined with spontaneous natural activity, translates into measurable electrical signals, offering insights into neural synchronisation and rhythmic patterns in the brain. Specifically, the output of the W-C model can be modelled as an LFP signal, expressed as a linear combination of the excitatory (E) and inhibitory (I) states, thereby capturing the interplay between these dynamics in the context of network activity.

It is essential to acknowledge that the W-C model has been widely validated as a reliable representation of population-level neural dynamics. Its ability to capture the interactions between excitatory and inhibitory subpopulations is consistent with the behaviour observed in cortical circuits [8, 31].

The W-C model demonstrates complex nonlinear dynamics, including phenomena such as multistability, hysteresis, and limit cycles. This rich repertoire of operating modes resembles observed responses in neural tissue, establishing a trade-off between the level of detail and the reduced degrees of freedom of the system. In this regard, is highly appreciated, specially for control purposes, that the model is able to forecast essential features of the dynamic behaviour while retaining low dimensionality. The system response is highly sensitive to the selection of parameters and input conditions. Figure 2 illustrates the open-loop response of the W-C system in the I-E phase space for varying levels of the excitatory input P. As the input increases, the system undergoes a notable qualitative transition in behaviour, shifting from damped oscillations, as shown in Figure 2a, to sustained oscillations in Figure 2c. Specifically, the response of the system to different values of P is depicted in panels (a–c), in Figure 2, corresponding to $P = 0$, $P = 0.4$, and $P = 0.8$, respectively. In Figure 2a, for

$P = 0$, the W-C system exhibits an isolated equilibrium point (with stable node structure) at the origin. With an increase to $P = 0.4$ in Figure 2b, the equilibrium shifts to a stable focus structure. Finally, in Figure 2c, for $P = 0.8$, the equilibrium has an unstable focus structure, leading to the emergence of oscillatory dynamics characterised by a limit cycle, outlined as the closed, isolated, and stable attractor in the phase space. An exhaustive study of the bifurcations can be found in [32].

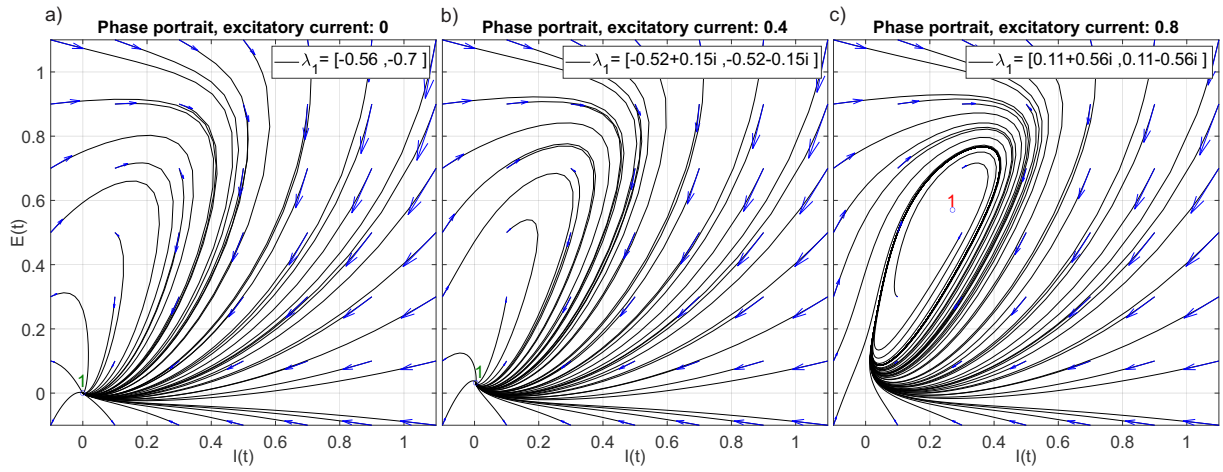

Figure 2. Open loop response of the W-C system for varying levels of excitatory current stimulus P, and eigenvalues of its jacobian matrices.

2.2 *Optogenetic actuation via light-sensitive ion channels*

The light-to-current mappings, considered as actuation channels to be attached to the W-C model, can be expressed as

$$\begin{aligned} \mathscr{O}_P &: L_P \longrightarrow P \\ \mathscr{O}_Q &: L_Q \longrightarrow Q. \end{aligned} \tag{2}$$

The mappings in Equation (2) can be defined either as algebraic relationships that link the applied light intensities L_P and L_Q with the resulting transmembrane currents P and Q, or as differential equations that capture the dynamic behaviour of opsins [33]. Specifically, for opsins such as ChR, as considered in the application case Section 4, the light-induced conductance has been shown to follow a first-order system approximation based on empirical studies [18]. The use of chirp signals to probe response of ChR in [18] shows a clear single cutoff frequency in the response spectrum, consistent with a first-order system, characterised by a time constant governing activation and deactivation kinetics. This first-order approximation can also be extended to NpHR, an inhibitory opsin known for its chloride ion transport mechanism. Like ChR, NpHR exhibits light-induced conformational changes that can be well-approximated by a single time constant for activation and deactivation [14].

The light-induced conductance dynamics of the ChR, NpHR-type pairs, driven by excitatory L_P and inhibitory L_Q light inputs, can be captured by the first-order differential equation:

$$\tau \frac{d}{dt} \begin{bmatrix} P \\ Q \end{bmatrix} + \begin{bmatrix} P \\ Q \end{bmatrix} = \begin{bmatrix} L_P \\ L_Q \end{bmatrix}, \tag{3}$$

where τ represents the time constant associated with the activation and deactivation of the opsin. This provides a convenient description of the opsin behaviour, where the output currents P and Q evolve in proportion to the input light stimuli and the

current state of the system. In particular, the cutoff frequency reported in [18] is $f_c \approx 100$ Hz, which corresponds to a time constant of $\tau \approx \frac{1}{100}$ s in Equation (3). This constitutes a unified approach for modelling both excitatory (ChR) and inhibitory (NpHR) opsins.

Previous studies [18] have demonstrated that the dynamics of opsins, such as ChR and NpHR, can be accurately approximated by first-order systems, providing a physiologically sound approach to modelling light-induced neural modulation. This unified framework, which integrates the kinetics of opsins and their interactions with neural circuits, ensures both mathematical coherence and biological relevance. Additionally, the flexibility of the model in including various optogenetic tools, while maintaining fidelity to observed dynamic properties, underscores its applicability across different experimental conditions, thus reinforcing its utility for simulating real-world neural control mechanisms.

Within this framework, the opsin dynamics can be incorporated into the system, providing a more detailed representation. However, when the opsin time constants are significantly faster than the main dynamics system, these relationships can be simplified or neglected without loss of generality [26].

3. Main results: Control

3.1 *Controller and estimator design*

Based on Equation (1), the W-C model can be rewritten in the following form:

$$\begin{bmatrix} \dot{E}(t) \\ \dot{I}(t) \end{bmatrix} = \begin{bmatrix} \frac{1}{\tau_E} & 0 \\ 0 & \frac{1}{\tau_I} \end{bmatrix} \left\{ - \begin{bmatrix} E(t) \\ I(t) \end{bmatrix} + \underbrace{\begin{bmatrix} f_E(\gamma_{xE} + P) \\ f_I(\gamma_{xI} + Q) \end{bmatrix}}_{u_{\mathrm{LTI}}(t)} \right\}, \tag{4}$$

with

$$u_{\mathrm{LTI}}(t) = \begin{bmatrix} \tilde{u}_1(t) \\ \tilde{u}_2(t) \end{bmatrix} = \begin{bmatrix} f_E(\gamma_{xe} + P) \\ f_I(\gamma_{xi} + Q) \end{bmatrix} \triangleq \begin{bmatrix} f_E(u_p) \\ f_I(u_q) \end{bmatrix}, \tag{5}$$

where the sigmoid activation function, as introduced in Equation (1), is defined as:

$$f_i(x) = \frac{1}{1 + e^{-a_i(x-\theta_i)}} - k_i, \quad k_i = \frac{1}{1 + e^{-a_i\theta_i}}, \tag{6}$$

with the constant k_i ensuring the range of $f_i(x)$ lies between $-k_i$ and $1 - k_i$. The chosen shape for this activation function is derived based on the unimodal distribution of neuronal firing thresholds. The corresponding inverse of this sigmoid function, required for the subsequent controller derivation, is given by:

$$x = -\frac{1}{a_i} \ln\left(\frac{1}{f_i + k_i} - 1\right) + \theta_i, \tag{7}$$

where $i \in \{E, I\}$, and a_i and θ_i represent the gain and threshold, respectively, as illustrated in Figure 3.

To simplify the analysis, refractory period terms in Equation (1) are omitted (i.e., $rp_E = rp_I = 0$), since they have a negligible influence on the system dynamics [9].

The system state consists of excitatory $E(t)$ and inhibitory $I(t)$ activities. The system output, the LFP, is modelled as a linear combination of these activities. This output can be expressed as:

$$y(t) = \begin{bmatrix} c_1 & c_2 \end{bmatrix} \begin{bmatrix} E(t) \\ I(t) \end{bmatrix}, \tag{8}$$

where c_1 and c_2 are constants determining the relative contributions of excitatory and inhibitory activities.

The terms $\gamma_{xi}(t)$ in Equations (4) and (5), are compactly defined as:

$$\begin{aligned} \gamma_{xE}(t) &= w_{EE}\hat{E}(t) - w_{EI}\hat{I}(t), \\ \gamma_{xI}(t) &= w_{IE}\hat{E}(t) - w_{II}\hat{I}(t), \end{aligned} \tag{9}$$

where $\hat{E}(t)$ and $\hat{I}(t)$ are estimates of the excitatory and inhibitory activities, respectively, which can be obtained using nonlinear estimation techniques, such as Kalman-based strategies [22]. While these activities could, in theory, be measured directly (e.g., through fluorescence techniques), this analysis assumes that only noisy voltage measurements (LFP), as given by the system output in Equation (8), are available. Briefly, the estimation process calculates the internal states of the system, given the system inputs and measurements. This is done iteratively, alternating between propagation and correction steps, to optimally combine the prediction produced by the mathematical model with the '*real-world*' (available) output of the system. In this study, the estimated states, $\hat{E}(t)$ and $\hat{I}(t)$, are computed using a standard implementation of the EKF[22], as illustrated in Figure 4. This observer is an adaptation of the classical Kalman filter designed to handle nonlinear models, with update steps relying on regular Jacobian linearisation around the current operating point.

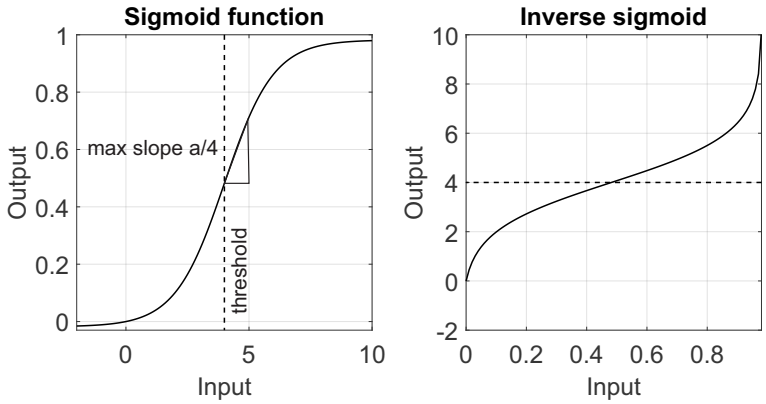

Figure 3. The sigmoid activation function and its inverse. The threshold θ_i is defined as the input value at which the slope of the curve reaches its maximum, $a_i/4$, where $i \in \{E, I\}$.

The manipulated inputs P and Q are given by:

$$\begin{aligned} \begin{bmatrix} u_E \\ u_I \end{bmatrix} &= \begin{bmatrix} u_p - \gamma_{xE} \\ u_q - \gamma_{xI} \end{bmatrix} \\ &= \begin{bmatrix} -\frac{1}{a_E} \ln\left(\frac{1}{u_1 + k_E} - 1\right) + \theta_E - \gamma_{xE} \\ -\frac{1}{a_I} \ln\left(\frac{1}{u_2 + k_I} - 1\right) + \theta_I - \gamma_{xI} \end{bmatrix}, \end{aligned} \tag{10}$$

where the terms u_1 and u_2 represent the components of the saturated control signal u_{sat} (refer to Figure 4), discussed in the following. The parameters γ_{xE} and γ_{xI} denote the feedback contributions from the excitatory and inhibitory activities of the system, respectively, and are calculated as described in Equation (9). The variables u_p and u_q are derived using the inverse sigmoid function outlined in Equation (7).

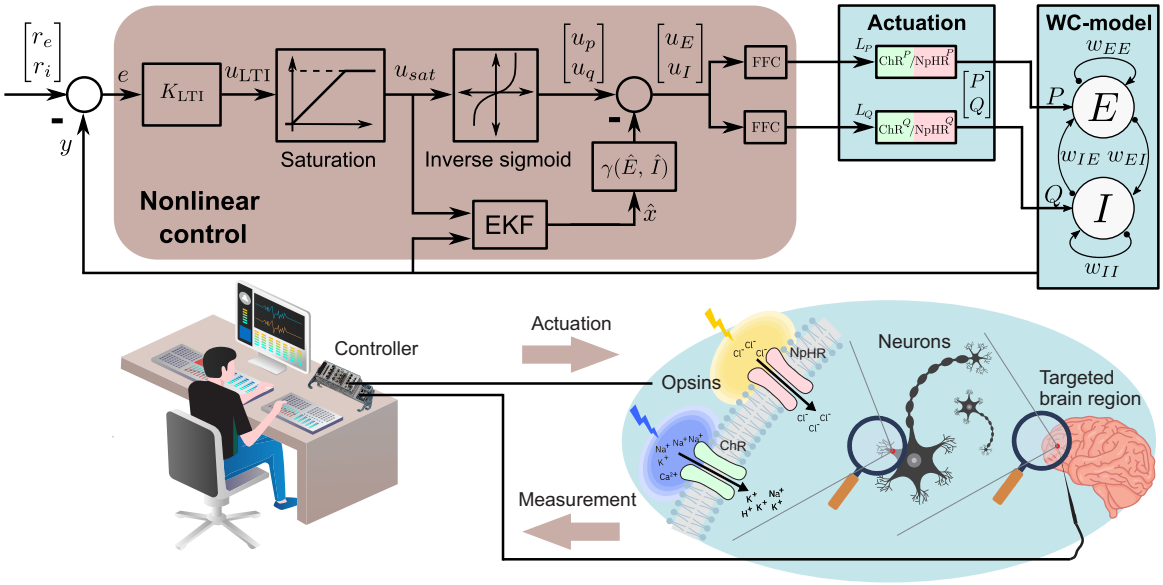

Figure 4. Nonlinear closed-loop control scheme based on the Wilson-Cowan equations. The block diagram illustrates the proposed algorithm connected to the opsin actuators and WC model. In the lower schematic, the experimental scenario for a potential implementation is detailed.

The stabilising controller K_{LTI} in Figure 4 is used to compute the control signal u_{LTI} based on the the error signal $e(t)$. This controller operates within the framework of the linear time-invariant (LTI) model, defined by Equations (4) and (8), and can be represented by a transfer matrix $G(s)$ in the Laplace domain. Thus, based on the model $G(s)$, the controller $K(s)$ can be designed as a standard LTI reference tracking controller. A key focus of this design is tracking oscillatory references, which are relevant to evoke biologically significant rhythms. Given the inherent uncertainty in complex biological systems, it is crucial to ensure that both robustness and performance are addressed to handle dynamic uncertainties [34, 35]. This concept will be further discussed in Section 3.2

The controller output, u_{LTI}, is expressed as a vector in Equation (5). The manipulated input signals u_E and u_I are then obtained using state estimation and Equation (10). Particularly, u_{sat} is related with u_p and u_q through the inverse sigmoid function in Equation (7). Similarly, the components of u_{LTI} in Equation (5), $\tilde{u}_j$, must remain within the range $[-k_i, 1-k_i]$. Therefore, the saturated control signal, $u_{sat}(t)$, is defined as follows:

$$u_{sat}(t) = \begin{cases} 1-k_i & \text{if} \quad \tilde{u}_j \geq 1-k_i, \quad (j=1,2) \\ -k_i & \text{if} \quad \tilde{u}_j \leq -k_i, \quad (j=1,2) \\ u_{\mathrm{LTI}}(t) & \text{otherwise} \end{cases}$$

Figure 5 shows how the LTI control signals are saturated within the interval $[-k_i, 1-k_i]$, resulting in the saturated control signals u_{sat}. From the definition of this saturation, the gain of the nonlinear operator is always less than one. Consequently, the small-gain theorem can be employed to demonstrate the closed-loop stability of the nonlinear system [34, 35].

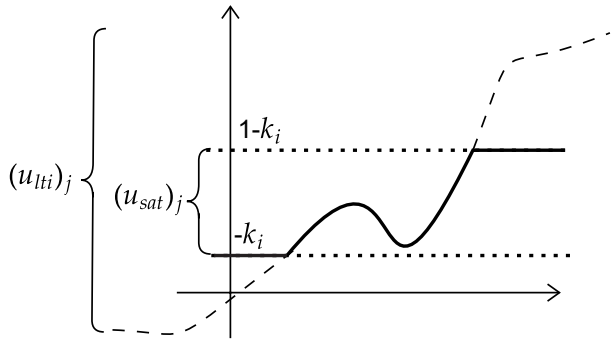

Figure 5. Linear time-invariant signals, $[\tilde{u}_1, \tilde{u}_2]^T$, versus saturated control signals, $[u_1, u_2]^T$.

Following the schematic representation in Figure 4, the resulting control signal mapping, based on the expression in Equation (3), can be obtained as follows:

$$\begin{bmatrix} u_E \\ u_I \end{bmatrix} \overset{\text{FFC (2nd order filter)}}{\longrightarrow} \begin{bmatrix} L_P \\ L_Q \end{bmatrix} \overset{\text{Opsin Dynamics ChR/NpHR}}{\longrightarrow} \begin{bmatrix} P \\ Q \end{bmatrix}. \tag{11}$$

Initially, the signal vector $\begin{bmatrix} u_E & u_I \end{bmatrix}^\intercal$, in Equation (10), is processed through the filter FFC, which is a second-order LTI system. This block is designed via a *feedforward* strategy resembling a lead and lag compensator [36], and is implemented to proactively modify the response of the actuator. Particularly, it cancels the opsin model single pole while adding two faster poles, and thus attenuating the actuator lag. The implementation of this feedforward scheme assumes that the opsin model is linear and time-invariant (LTI), therefore the feedforward block parameters remain fixed, as the dynamics of the system do not require adaptive tuning or weight updates. This approach ensures a more agile system response while maintaining stability, as illustrated in Figure 8. By incorporating this lead and lag structure, the FFC filter enhances the ability of the system to handle high-frequency dynamics (typically around 100 Hz) observed in the local field potential spectral content, while maintaining stability and robustness in the overall control strategy. The output of this stage yields the signals $\begin{bmatrix} L_P & L_Q \end{bmatrix}^\intercal$. Subsequently, these signals are directed to the opsin filter, which comprises the ChR and NpHR channels. The relationship between the signals $\begin{bmatrix} L_P & L_Q \end{bmatrix}^\intercal$ and the final output signals $\begin{bmatrix} P & Q \end{bmatrix}^\intercal$ is governed by the first-order differential equation in (3). This structured mapping delineates the flow of signals from the initial inputs through the filtering processes, culminating in the biologically relevant output signals. It highlights the importance of each transformation in the overall signal processing framework. It is important to emphasise that both signals P and Q can produce either excitatory or inhibitory effects, depending on their sign (positive or negative magnitude). Specifically, when P and Q are positive, they exhibit excitatory effects, while negative values result in inhibitory behaviour. Due to the strong synaptic coupling between the E and I subpopulations in the W-C model, as shown in Figure 1, a positive value in signal P can indirectly induce inhibitory behaviour in the I subpopulation. Similarly, this relationship applies to signal Q and the E subpopulation. This scenario is indicated in Figure 4 with the superscripts P and Q in the blocks ChR/NpHR. Thus, in Figure 4, the excitatory and inhibitory behaviours are schematically depicted using red and green blocks. To provide a broader perspective on advanced control strategies, particularly those utilising disturbance rejection and feedforward approaches, readers interested in FFC methodologies may refer to studies like [37], which explore multilayer neurocontrol for high-order uncertain nonlinear systems with active disturbance rejection. However, a significant gap remains in their application to neurophysiological systems, which underscores the novelty of our proposed methodology.

3.2 *Stability and robustness analysis*

The previously discussed LTI model, $G(s) : u_{\mathrm{LTI}} \to y$, represents a diagonal multiple-input, multiple-output (MIMO) system. Although u_{LTI} is nonlinear with respect to (P, Q), robust control techniques can generally be applied to handle MIMO nonlinear uncertain systems. Therefore, the closed-loop system depicted in Figure 4 can be reformulated as an LTI model coupled with a bounded "uncertainty" block $\Delta = \mathrm{diag}\{\Delta_E, \Delta_I\}$, replacing the nonlinearity of the system with this LTI representation and a bounded uncertainty block (In this study, the dynamical uncertainty replaces the original nonlinearity with an LTI model and a bounded Δ block. However, this approach can also model systems with uncertain nonlinear dynamics.).

The Δ operator is defined as follows:

$$\Delta_i \triangleq \begin{cases} u_{\delta_j} = \tilde{u}_j > 1 - k_i & \to \quad y_{\delta_j} = -\tilde{u}_j + 1 - k_i, (j = 1,2) \\ u_{\delta_j} = \tilde{u}_j \in [-k_i, 1 - k_i] & \to \quad y_{\delta_j} = 0, (j = 1,2) \\ u_{\delta_j} = \tilde{u}_j < -k_i & \to \quad y_{\delta_j} = -\tilde{u}_j - k_i, (j = 1,2). \end{cases} \tag{12}$$

Thus, Equation (12) characterises the difference between u_{LTI} and u_{sat}, as illustrated by the dashed line in Figure 5. By definition, the gain of the $\Delta : u_\delta \to y_\delta$ operator satisfies $\|\Delta\| \leq 1$.

Considering the complementary sensitivity function, which is the LTI closed-loop transfer matrix:

$$T(s) = K_{\mathrm{LTI}}(s)G(s)\left[I + K_{\mathrm{LTI}}(s)G(s)\right]^{-1}, \tag{13}$$

shown schematically in Figure 6, the internal stability of the overall system can be established, as discussed in the following.

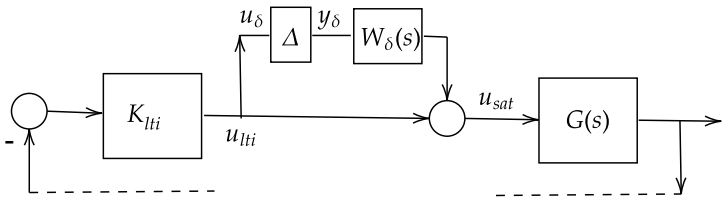

Figure 6. Block structure used for analysing the closed-loop stability of the nonlinear system.

The same approach can be extended to include dynamic uncertainty, represented by a filter $W_\delta(s)$ in series with Δ, as shown in Figure 6. According to standard robust control theory results [34, 35], derived from the small-gain theorem, the necessary and sufficient condition for stability is:

$$\|W_\delta(s)T(s)\|_\infty < 1. \tag{14}$$

The expression in Equation (14) ensures nominal closed-loop stability for the nonlinear saturation when $W_\delta = 1$ and provides robust stability in the presence of dynamic uncertainty, where $W_\delta(s)$ accounts for model uncertainty. This analysis assumes a small estimation error, which affects the control signal u_{sat}. Based on the definitions in Equation (9), the error $\delta u = u_{sat} - \hat{u}_{sat}$ can be bounded as follows:

$$\delta u \quad = \quad f(\delta x) = \begin{bmatrix} f_E\left(W_{EE}\delta E(t) - W_{EI}\delta I(t)\right) \\ f_I\left(W_{IE}\delta E(t) - W_{II}\delta I(t)\right) \end{bmatrix},$$

where $\delta E = E - \hat{E}$ and $\delta I = I - \hat{I}$ represent the estimation errors. The worst-case scenario occurs at the maximum slope of the sigmoid function $f(x)$, specifically when $x_{wc} = \theta$, meaning $f(x_{wc}) = 0.5 - k$. Therefore, the error under the worst-case condition is:

$$(\delta u)_{wc} = (0.5 - k) \begin{bmatrix} W_{EE} & -W_{EI} \\ W_{IE} & -W_{II} \end{bmatrix} \begin{bmatrix} \delta E \\ \delta I \end{bmatrix}. \tag{15}$$

Consequently, a simplified implementation should ensure that this value does not significantly affect the control signal u_{sat}, specifically verifying that $\frac{\|(\delta u)_{wc}\|}{\|u_{sat}\|} < \xi_e$, where ξ_e is a predefined small threshold.

For a more advanced solution, one could introduce an additional uncertainty block $\hat{\Delta}$, which would act on u_{sat} as shown in Figure 6, with the Kalman filter error $\delta x = \delta y = (y - \hat{y})$ serving as its input. In this case, the robust stability condition would rely on the structured singular value $\mu_{\mathbf{\Delta}}$, with the structure $\mathbf{\Delta} = \text{diag}(\Delta, \hat{\Delta})$, instead of the previous condition based on the $\mathscr{H}_\infty$ norm described in Equation (14). However, a detailed exploration of this approach is beyond the scope of the current work.

In this discussion, it is important to note that the stability and robustness analysis described can still be applied even when the model is combined with the actuation scheme considered in this study, which includes the ChR/NpHR and FFC blocks. In addition to the theoretical framework presented, the stability of the combined system, incorporating the dynamics of the ChR/NpHR actuation system and the FFC filter, is further examined in this study through exhaustive simulation. This approach provides a practical means of validating the theoretical predictions and ensuring that the system behaves as expected under a variety of operational conditions. Exhaustive simulations allow for exploring the response of the system across a wide range of parameters, including variations in input signals, feedback gains, and environmental disturbances. By systematically varying these parameters, potential stability issues can be identified, that may not be evident through analytical methods alone. The simulations can help assess the performance of the system in the presence of nonlinearities, time delays, and uncertainties inherent in biological systems. To conduct these simulations, the model is implemented using numerical methods, where the dynamics of each component, specifically the LTI system, the FFC filter, and the ChR/NpHR actuation, are accurately represented.

3.3 *General limitations*

One important limitation of the proposed framework is its reliance on the opsin dynamics obtained from a previously published study [18]. These dynamics, while providing a solid foundation, may not exactly match the true biological behaviour under varying experimental conditions. Consequently, the inverse model included in the controller may only partially represent these dynamics, potentially affecting control accuracy. This issue, and similar aspects, has been addressed in a related review study by the authors [6]. Additionally, the following broader limitations inherent to the LTI-based control method when applied to the W-C model can be mentioned. Firstly, the framework may not fully capture unmodelled dynamics or external disturbances, as LTI-based approaches are sensitive to model inaccuracies. This limitation could lead to degraded performance in scenarios where the system is exposed to unknown perturbations or parameter variations. Secondly, the W-C model, while computationally efficient and biologically inspired, abstracts complex neural dynamics into a low-dimensional framework. This abstraction might overlook critical higher-dimensional dynamics present in real neural circuits, which could influence the overall system behaviour and control performance. Lastly, the proposed control approach does not include adaptive mechanisms or strategies to handle unexpected changes in neural dynamics, limiting its resilience under non-ideal conditions.

4. Illustrative example: Reference tracking control using real brain signals

This section presents an example of reference tracking control tackled by the W-C model coupled with actuation channels. In this example, the controlled closed-loop system should track experimentally acquired signals from real brain activity. These reference signals, denoted as $s_1(t)$, $s_2(t)$, and $s_3(t)$, are LFPs from mice motor cortex, as discussed in [23].

These signals, offer key insights into neural dynamics and present a realistic challenge for the control framework due to their distinct temporal and spectral characteristics. Particularly, the main features of the reference signals are found in their spectral content. Specifically, $s_1(t)$ has two prominent peaks in the frequency domain, located at approximately 10 Hz and 20 Hz; $s_2(t)$ exhibits two primary components around 1 Hz and 7 Hz; and $s_3(t)$ features a significant spectral peak at 3 Hz. Figure 7a1–3 illustrates the traces of $s_1(t)$, $s_2(t)$, and $s_3(t)$, capturing the temporal variations of the brain signals, where the time-domain signals are represented as xV, indicating a scaled magnitude of the acquired signal in volts.

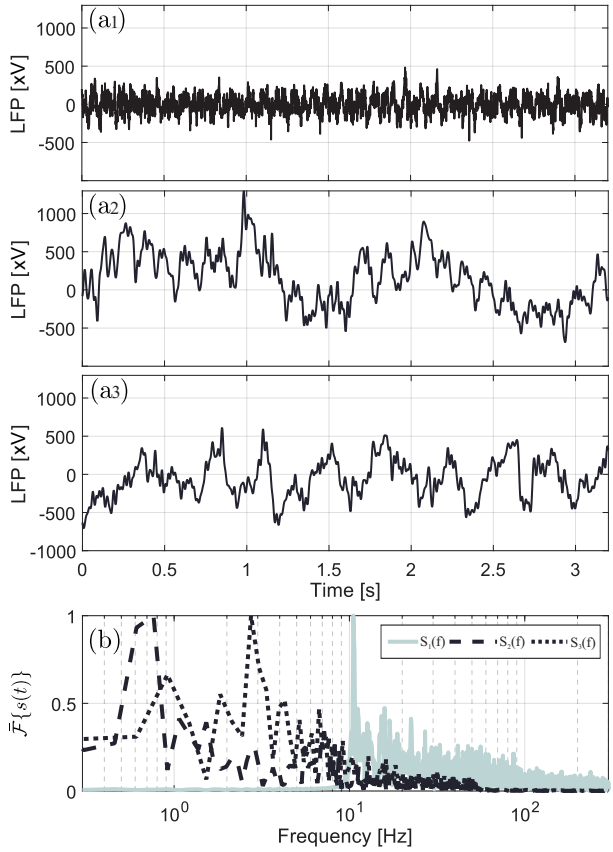

Figure 7. Reference signals considered for tracking. (**a1–3**) Time domain traces of $s_1(t)$, $s_2(t)$, and $s_3(t)$, respectively. (**b**) Normalised Fourier transforms of $s_1(t)$, $s_2(t)$, and $s_3(t)$, showing key frequency components.

Figure 7b shows the corresponding normalised Fourier transforms of these signals (unitary magnitude), clearly identifying their key frequency components. The normalisation to one in Figure 7b allows for easier comparison across the different signals and highlights the prominent spectral peaks that play a crucial role in designing the control strategy.

4.1 *Controller design*

4.1.1 *Opsin dynamics and feedforward control*

To implement the controller based on these reference signals, the dynamics of optogenetic actuators are considered. These opsins are light-sensitive proteins used to modulate neuronal activity by either exciting or inhibiting specific neuronal populations in response to light stimuli.

The frequency response of the opsin channels, taken from [18], which captures the dynamics of how they react to light inputs, is approximated and shown in Figure 8. For simplicity, only the frequency response of ChR is depicted, as the response of NpHR is similar and omitted for clarity. The feedforward compensator (FFC) is applied to precondition

the input signal to ensure better control performance. As explained in Section 3, considering the opsin first order transfer function

$$O(s) = \frac{2\pi \times 100}{(s + 2\pi \times 100)}, \tag{16}$$

and choosing FFC block as

$$FFC(s) = \frac{2.0480 \times 10^8 O^{-1}(s)}{(s + 7000)^2}, \tag{17}$$

effectively cancels the opsin pole, while adding faster poles to modify the overall frequency response, allowing the control system to track the reference signals more accurately. Figure 8 shows the Bode plots of both the opsin dynamics and the FFC, along with the coupled opsin plus precompensation frequency response, highlighting the adjustments made to the frequency response to improve tracking across the frequency ranges of interest.

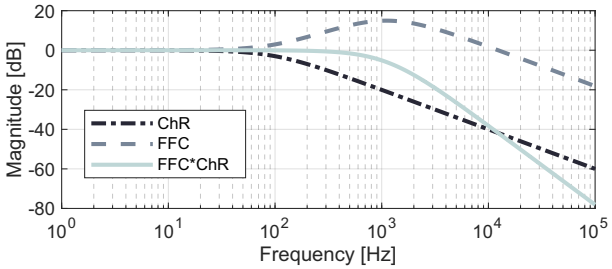

Figure 8. Frequency response of the opsin dynamics and precompensation using the feedforward compensator (FFC). The frequency response for ChR is shown, with NpHR assumed to exhibit similar behaviour.

4.1.2 *WC dynamics and feedback control*

The values of τ_E and τ_I are physiologically constrained to be positive, ensuring that the LTI system $G(s)$ is inherently stable and has minimum phase characteristics. Furthermore, since the interaction between subpopulations is captured within the sigmoid functions (represented by the input term u_{LTI}), the formulation in (4) effectively decouples the state variables E and I. As a result, this system structure is suitable for control synthesis approaches tailored to open-loop stable systems, allowing for the independent design of single-input, single-output (SISO) controllers K_I and K_E for each state variable. These controllers modulate the inputs u_E and u_I, and subsequently the inputs P and Q, which in turn shift the activity levels of the corresponding sub-populations to achieve the desired output behaviour as expressed in (8).

The proposed controller design is built upon the internal model control (IMC) framework for stable systems [38]. The controller structure employs q-parameterisation, represented as:

$$K_{\text{LTI}}(s) = q(s)\left[I - q(s)G(s)\right]^{-1}, \tag{18}$$

where $q(s)$ is given by:

$$q(s) = F(s)G(s)^{-1}. \tag{19}$$

Here, $F(s)$ is the design parameter, chosen as a low-pass filter to ensure stability and render $q(s)$ realisable. The resulting closed-loop transfer function, also known as the complementary sensitivity function, is:

$$T(s) = q(s)G(s) = F(s). \tag{20}$$

To track specific reference signals within a desired frequency bandwidth, $F(s)$ is selected to achieve unity gain in that range. For example, $F(s) = \frac{500}{s+500}$ ensures $T(j2\pi \times 10\,\text{Hz}) \approx 0\,\text{dB}$. Applying this $F(s)$ in the above framework yields stabilising controllers in the following form:

$$K_{\text{LTI}}(s) \triangleq \begin{bmatrix} K_E(s) & 0 \\ 0 & K_I(s) \end{bmatrix} = \begin{bmatrix} \frac{5(s+1)}{s} & 0 \\ 0 & \frac{10(s+0.5)}{s} \end{bmatrix}. \tag{21}$$

The chosen $F(s)$ reflects the assumption that the system requires precise reference tracking in a specific bandwidth while maintaining stability. This ensures robustness to potential modelling inaccuracies.

These controllers, designed as discussed earlier, are integrated with the inverse sigmoid function and the state estimation process to form a nonlinear controller. These outputs of the controller, $\begin{bmatrix} u_E & u_I \end{bmatrix}^{\mathsf{T}}$, can then be applied optically, through the FFC structure, as shown in Figure 4.

4.2 *Simulations*

In this section, the closed-loop pattern synchronisation problem, to illustrate the effectiveness of the proposed control framework, is studied. The patterns analysed correspond to brain rhythms categorised by their oscillation frequencies. This example specifically highlights cross-frequency coupling [39], showcasing a top-down interaction among different frequency bands: low-frequency delta oscillations (between 1 Hz and 3 Hz), represented by $s_3(t)$; theta oscillations (ranging from 4 Hz to 12 Hz), denoted as $s_2(t)$; and high-frequency gamma oscillations (up to approximately 100 Hz), indicated by $s_1(t)$. The theta rhythm is known to modulate the gamma power of intracortical LFP [40], acting as a transient coordination mechanism across different brain regions [41], which is crucial for cognitive communication. Notably, deficits in this coupling have been associated with conditions such as Alzheimer's disease [42], highlighting the potential of the presented strategy as a therapeutic avenue.

4.2.1 *Closed-loop performance analysis: Dual vs. single opsin control scenarios*

In this illustrative example, the closed-loop performance is studied under two distinct scenarios. In the first scenario, both excitatory and inhibitory opsins (ChR and NpHR) are utilised in the control loop, allowing the system to modulate neural activity by either exciting or inhibiting neuronal populations as required by the reference signals. In the second scenario, only the excitatory type opsin (ChR) is considered, with the action of the inhibitory opsins (NpHR) being cancelled. This comparative assessment methodology provides a clear understanding of the performance and its limitations when control is exerted through a single-type opsin. By contrasting these two scenarios, the analysis explores the full potential of using both excitatory and inhibitory channels for richer control and the trade-offs associated with relying on only excitatory drive in the feedback loop.

The results are firstly presented when considering both excitatory and inhibitory opsins, as shown in Figure 9. The outcomes in Figure 9a illustrate the closed-loop response of the system when forcing $s_1(t)$, the one in Figure 9b corresponds to signal $s_2(t)$, and the one in Figure 9c represents the response using $s_3(t)$. The reference signal for each subpopulation r_E, r_I is designed based on the assumption that the output LFP is modelled as the weighted summation of both activities, that is $y(t) = E - I$. Therefore the r_E (r_I) is used to conform the positive (negative) part of the desired signal to be forced in the system. Consequently, in Figure 9, the resulting reference signal, defined as the difference $r_E - r_I$, is depicted with a dashed black line, while the closed-loop output $y(t) = E - I$ is shown with a grey solid line. When both opsins are considered, the system demonstrates a remarkable level of performance, effectively replicating the primary oscillatory components present in the reference signals. Furthermore, the high-frequency components, potentially regarded as noisy exogenous factors, are effectively filtered out from the system output, showcasing the robustness of the implemented control methodology despite noise interference.

In contrast, the performance of the system when only excitatory opsins are utilised, as presented in Figure 10, is assessed.

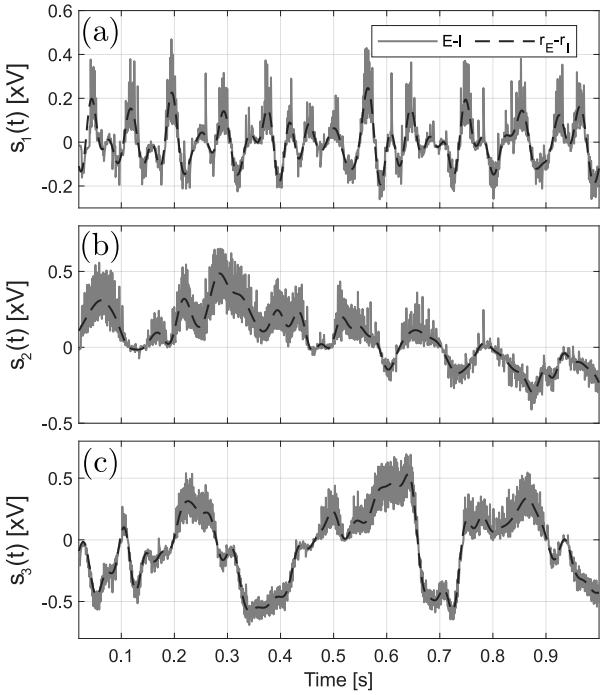

Figure 9. Results considering both opsins for the three reference signals $s_1(t)$, $s_2(t)$, and $s_3(t)$.

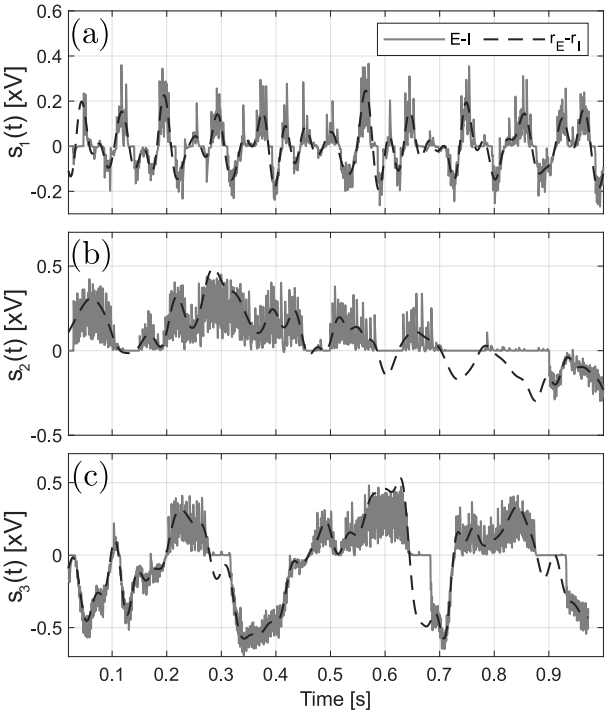

Figure 10. Results considering only excitatory opsins for the three reference signals $s_1(t)$, $s_2(t)$, and $s_3(t)$.

The structure of Figure 10 is similar to the case of Figure 9, with the top (a), middle (b), and bottom (c) plots corresponding to reference signals $s_1(t)$, $s_2(t)$, and $s_3(t)$, respectively. Although the system can successfully replicate the fundamental oscillatory behaviour (reference) with excitatory opsins, limitations arise in accurately reproducing

the complete oscillatory profile, particularly showing saturation effects during some half-cycles of the response. It is hypothesised that this limitation is due to the inability of driving the voltage to hyperpolarised values relying on the excitatory coupling alone. It is especially pronounced for reference signals s_2 and s_3, while for $s_1(t)$ this effect can be virtually neglected.

In addition, to assess the tracking performance of the proposed control strategy, simulations are conducted using sinusoidal reference signals with varying amplitudes and frequencies. The input reference signals were defined with amplitudes ranging from 0.1 to 1 V and frequencies between 1 Hz and 100 Hz. Each simulation is executed for a duration of 1 s with a sampling time of $T_m = 10^{-4}$ s.

The tracking error is defined as $e(t) = y(t) - r(t)$, with $y(t)$ and $r(t)$ the closed-loop output and the desired reference signal, respectively. The mean squared error (MSE) [43], computed for each simulation as:

$$\text{MSE} = \frac{1}{N}\sum_{i=1}^{N} e(i)^2, \tag{22}$$

where N is the total number of data points, and $e(i)$ represents the error at each time step i, quantifies the cumulative tracking error. Thus, the MSE metric is used as the primary performance metric to evaluate the control system's tracking ability. If the control strategy could achieve perfect tracking, the system output would be identically equal to the input, achieving zero error accordingly. However, in practice, discrepancies arise during both transient and stationary regimes of the system, making the MSE metric particularly useful to capture performance issues over time.

Figure 11 shows the MSE as a function of both frequency and amplitude, providing a comprehensive view of the system's performance across the specified range of operating conditions.

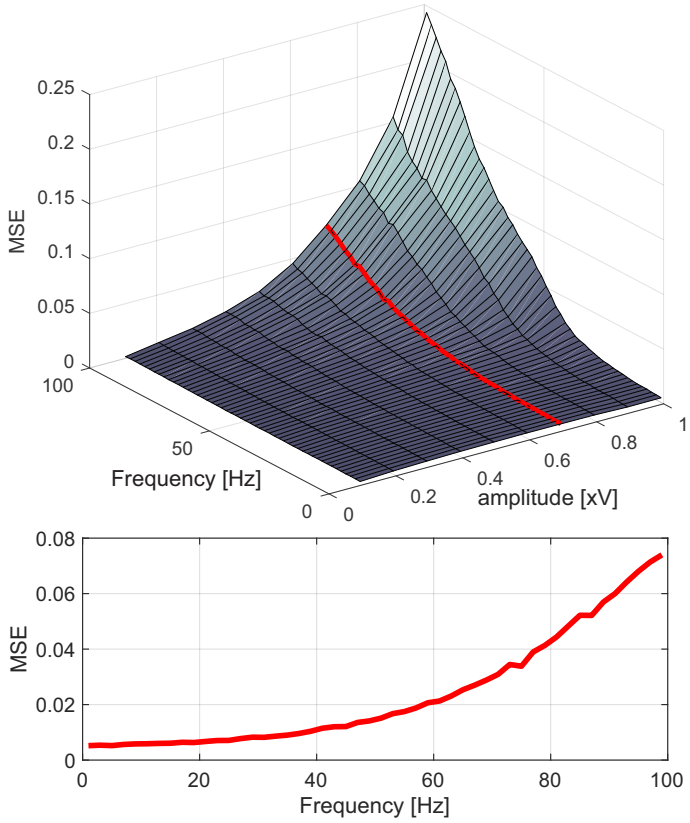

Figure 11. MSE of the tracking performance as a function of frequency (1 Hz to 100 Hz) and amplitude (0.1 V to 1 V), presented in its original linear scale. The red curve highlights the system's response for a fixed amplitude of 0.7 V.

In particular, the red curve highlights the tracking performance of the system for a fixed amplitude of 0.7 V, allowing for comparison across different frequencies while holding the amplitude constant.

To enhance the visualisation of the MSE, the error metric was also expressed in decibels (dB), as shown in Figure 12.

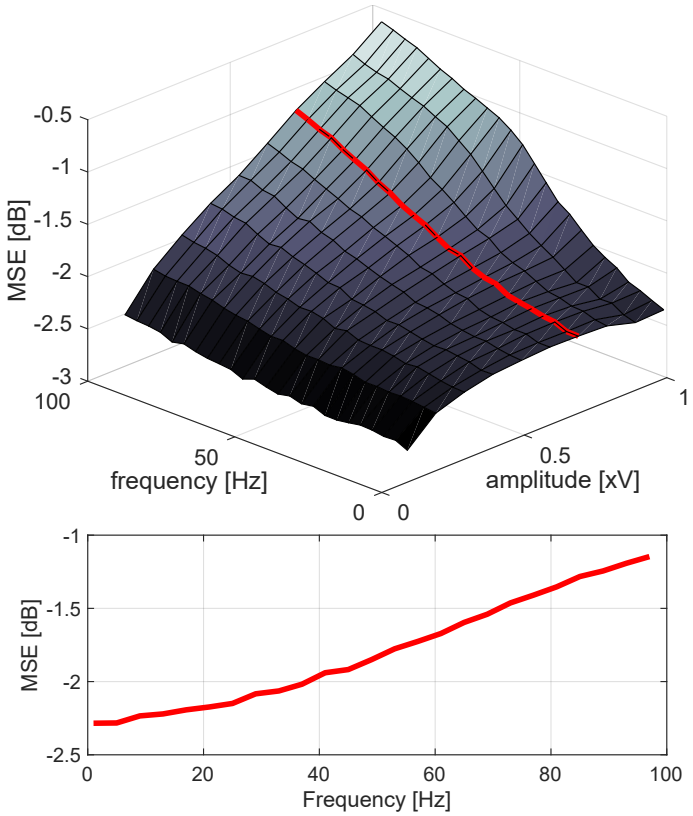

Figure 12. MSE of the tracking performance as a function of frequency (1 Hz to 100 Hz) and amplitude (0.1 V to 1 V), presented in decibels (dB). The red curve highlights the response of the system for a fixed amplitude of 0.7 V.

The transformation to a logarithmic scale is commonly used in signal processing to compress large dynamic ranges and provide more intuitive insights into relative error levels. Presenting the MSE in dB compresses the error range, making small variations easier to detect and highlighting performance trends, particularly at low amplitudes, which are harder to see on a linear scale. The MSE in dB provides clearer insight into these variations, particularly at lower frequencies where the tracking error is minimal but still significant.

It can be seen in Figures 11 and 12, that the system maintains good tracking performance across a wide range of frequencies and amplitudes. However, as the frequency increases, the MSE generally rises, indicating that the control system struggles to maintain precise tracking at higher frequencies. This behaviour is consistent across all amplitudes, although the magnitude of the error varies depending on the input signal amplitude.

5. Conclusions

This study presents a neuromodulation approach including the following contributions. First, a novel robust approach to closed-loop control is proposed by integrating the W-C model with optogenetic actuation dynamics. Second, the implementation of an extended Kalman filter for state estimation, enables a nuanced understanding of the dynamics involved in neural modulation, and suggests that epiphenomenal measurements such as local field potentials (LFPs) are enough to decode internal states. Third, by leveraging both excitatory (ChR) and inhibitory (NpHR) opsins within a control

framework, the research demonstrates the potential for inducing specific brain rhythms with high precision, based on real neural activity data. Fourth, the illustrative example effectively contrasts the performance of dual vs. single opsin-type control scenarios, revealing significant differences in tracking capability and overall efficacy.

The findings underscore the limitations of using only one opsin type, such as ChR, in the feedback loop, which may compromise the ability of the system to respond appropriately to varying reference signals. The comparative analysis emphasises the advantages of a dual opsin approach, paving the way for more sophisticated modulation strategies that can better mimic natural neural behaviours.

This methodology not only addresses the complexities of neural interactions but also highlights the necessity of incorporating both excitatory and inhibitory channels to achieve increased performance in closed-loop systems. Furthermore, the addition of an estimation framework for the system states reduces the gap between this preliminary study and a practical implementation of the control methodology, demonstrating that direct state measurements are not necessary.

To further support the robustness of the proposed control strategy, the tracking performance is evaluated across varying frequencies and amplitudes. The results demonstrate that the system maintains good performance across a wide range of conditions, although higher frequencies lead to increased MSE, indicating challenges in precise tracking at these frequencies as a limitation. These findings underscore the versatility and effectiveness of the control strategy across dynamic scenarios.

It is important to note that, the proposed ad-hoc nonlinear methodology combines dynamic inversion and robust control, tailored for neurophysiological systems. While broader comparisons, such as with unfalsified control [44], are beyond this study's scope, stability and robustness analyses confirm the effectiveness in this specific context of the presented approach.

Ultimately, the incorporation of realistic experimental setups into the control design marks a critical advancement in the field of closed-loop neuroscience. Future work will focus on refining the control strategies, expanding the range of applications for this framework, and exploring the translation of these findings into clinical settings. By integrating control system theory with neurophysiology, this study lays the groundwork for further innovations in the treatment of neurological disorders, enhancing our understanding of brain function through precise modulation techniques.

Acknowledgements

This research has been financially supported by grant PICT2017-2417 from the ANPCyT, Argentina.

Conflict of interest

We have no conflicts of interest to disclose.

References

[1] E. H. Kim, G. Chin, G. Rong, K. E. Poskanzer, and H. A. Clark, "Optical probes for neurobiological sensing and imaging," *Acc. Chem. Res.*, vol. 51, no. 5, pp. 1023–1032, 2018.

[2] J. Deubner, P. Coulon, and I. Diester, "Optogenetic approaches to study the mammalian brain," *Curr. Opin. Struct. Biol.*, vol. 57, pp. 157–163, 2019.

[3] K. B. Mirza, C. T. Golden, K. Nikolic, and C. Toumazou, "Closed-loop implantable therapeutic neuromodulation systems based on neurochemical monitoring," *Front. Neurosci.*, vol. 13, p. 808, 2019.

[4] D. Garcia-Violini, R. Sánchez-Peña, M. Moscoso-Vásquez, and F. Garelli, "Non-pharmaceutical intervention to reduce covid-19 impact in argentina," *ISA Trans.*, vol. 124, pp. 225–235, 2022.

[5] H. Joshi, "Mechanistic insights of covid-19 dynamics by considering the influence of neurodegeneration and memory trace," *Phys. Scr.*, vol. 99, no. 3, p. 035254, 2024.

[6] S. Martínez, D. García-Violini, M. Belluscio, J. Piriz, and R. Sánchez-Peña, "Dynamical models in neuroscience from a closed-loop control perspective," *IEEE Rev. Biomed. Eng.*, vol. 16, pp. 706–721, 2022.
[7] S. Coombes, "Next generation neural population models," *Front. Appl. Math. Stat.*, vol. 9, p. 1128224, 2023.
[8] H. R. Wilson and J. D. Cowan, "Excitatory and inhibitory interactions in localized populations of model neurons," *Biophys. J.*, vol. 12, no. 1, pp. 1–24, 1972.
[9] H. R.. Wilson, J. D. Cowan, "Evolution of the Wilson-Cowan equations," *Biol. Cybern.*, vol. 115, no. 6, pp. 643–653, 2021.
[10] F. Wendling, E. Koksal-Ersoz, M. Al-Harrach, M. Yochum, I. Merlet, G. Ruffini, F. Bartolomei, and P. Benquet, "Multiscale neuro-inspired models for interpretation of eeg signals in patients with epilepsy," *Clin. Neurophysiol.*, vol. 161, pp. 198–210, 2024.
[11] E. D. Dimwamwa, A. Pala, V. Chundru, N. C. Wright, and G. B. Stanley, "Dynamic corticothalamic modulation of the somatosensory thalamocortical circuit during wakefulness," *Nat. Commun.*, vol. 15, no. 1, p. 3529, 2024.
[12] K. Deisseroth, "Optogenetics," *Nat. Methods*, vol. 8, no. 1, pp. 26–29, 2011.
[13] V. Emiliani, E. Entcheva, R. Hedrich, P. Hegemann, K. R. Konrad, C. Lüscher, M. Mahn, Z.-H. Pan, R. R. Sims, J. Vierock, et al., "Optogenetics for light control of biological systems," *Nat. Rev. Methods Primers*, vol. 2, no. 1, p. 55, 2022.
[14] O. Yizhar, L. E. Fenno, T. J. Davidson, M. Mogri, and K. Deisseroth, "Optogenetics in neural systems," *Neuron*, vol. 71, no. 1, pp. 9–34, 2011.
[15] S. Sridharan, M. A. Gajowa, M. B. Ogando, U. K. Jagadisan, L. Abdeladim, M. Sadahiro, H. A. Bounds, W. D. Hendricks, T. S. Turney, I. Tayler, et al., "High-performance microbial opsins for spatially and temporally precise perturbations of large neuronal networks," *Neuron*, vol. 110, no. 7, pp. 1139–1155, 2022.
[16] H. Bansal, N. Gupta, and S. Roy, "Comparison of low-power, high-frequency and temporally precise optogenetic inhibition of spiking in nphr, enphr3.0 and jaws-expressing neurons," *Biomed. Phys. Eng. Express*, vol. 6, no. 4, p. 045011, 2020.
[17] F. Zhang, L.-P. Wang, E. S. Boyden, and K. Deisseroth, "Channelrhodopsin-2 and optical control of excitable cells," *Nat. Methods*, vol. 3, no. 10, pp. 785–792, 2006.
[18] D. Keppeler, R. M. Merino, D. Lopez de la Morena, B. Bali, A. T. Huet, A. Gehrt, C. Wrobel, S. Subramanian, T. Dombrowski, F. Wolf, et al., "Ultrafast optogenetic stimulation of the auditory pathway by targeting-optimized chronos," *EMBO J.*, vol. 37, no. 24, p. e99649, 2018.
[19] G. Acharya, S. F. Ruf, and E. Nozari, "Brain modeling for control: A review," *Front. Control Eng.*, vol. 3, p. 1046764, 2022.
[20] M. F. Singh, M. W. Cole, T. S. Braver, and S. Ching, "Developing control-theoretic objectives for large-scale brain dynamics and cognitive enhancement," *Annu. Rev. Control*, vol. 54, pp. 363–376, 2022.
[21] Y. Tian, S. Saradhi, E. Bello, M. D. Johnson, G. D'Eleuterio, M. R. Popovic, and M. Lankarany, "Model-based closed-loop control of thalamic deep brain stimulation," *Front. Netw. Physiol.*, vol. 4, p. 1356653, 2024.
[22] M. I. Ribeiro, "Kalman and extended kalman filters: Concept, derivation and properties," *Inst. Syst. Robot.*, vol. 43, p. 46, 2004.
[23] S. Martínez, R. S. Sánchez-Peña, and D. García-Violini, "Controlling neural activity: LPV modelling of optogenetically actuated Wilson–Cowan model," *J. Neural Eng.*, vol. 21, no. 3, p. 036002, 2024.
[24] N. Faedo, D. García-Violini, and J. V. Ringwood, "Controlling synchronization in a complex network of nonlinear oscillators via feedback linearisation and $\mathscr{H}_\infty$-control," *Chaos, Solitons Fractals*, vol. 144, p. 110722, 2021.
[25] J. Vezoli, L. Magrou, R. Goebel, X.-J. Wang, K. Knoblauch, M. Vinck, and H. Kennedy, "Cortical hierarchy, dual counterstream architecture and the importance of top-down generative networks," *Neuroimage*, vol. 225, p. 117479, 2021.
[26] S. Martinez, R. S. Sánchez-Peña, M. Belluscio, J. Piriz, and D. García-Violini, "Towards an experimental control of neural activity: The Wilson-Cowan model," *IFAC-PapersOnLine*, vol. 55, no. 40, pp. 223–228, 2022.
[27] A. Isidori, *Nonlinear Control Systems: An Introduction*, Heidelberg, Germany: Springer, 1985.
[28] V. I. Utkin, "Sliding mode control design principles and applications to electric drives," *IEEE Trans. Ind. Electron.*, vol. 40, no. 1, pp. 23–36, 1993.
[29] M. Vidyasagar, *Nonlinear Systems Analysis*, Philadelphia, PA, USA: SIAM, 2002.
[30] R. K. Powers and M. D. Binder, "Input-output functions of mammalian motoneurons," *Rev. Physiol. Biochem. Pharmacol.*, vol. 143, pp. 137–263, 2001.

[31] G. Deco, V. K. Jirsa, and A. R. McIntosh, “Emerging concepts for the dynamical organization of resting-state activity in the brain,” *Nat. Rev. Neurosci.*, vol. 12, no. 1, pp. 43–56, 2011.
[32] B. Pietras, “Modeling phase synchronization of interacting neuronal populations: from phase reductions to collective behavior of oscillatory neural networks,” Ph.D. thesis, Lancaster Univ., Lancaster, UK, 2018.
[33] J. C. Williams, J. Xu, Z. Lu, A. Klimas, X. Chen, C. M. Ambrosi, I. S. Cohen, and E. Entcheva, “Computational optogenetics: empirically-derived voltage-and light-sensitive channelrhodopsin-2 model,” *PLoS Comput. Biol.*, vol. 9, no. 9, p. e1003220, 2013.
[34] K. Zhou, J. C. Doyle, and K. Glover, *Robust and Optimal Control*, Tappan, NJ, USA: Prentice-Hall, 1996.
[35] R. S. Sánchez Peña and M. Sznaier, *Robust Systems Theory and Applications*, Hoboken, NJ, USA: John Wiley & Sons, 1998.
[36] G. C. Goodwin, S. F. Graebe, M. E. Salgado, *Control System Design*, Hoboken, NJ, USA: Prentice Hall, 2001; vol. 240.
[37] G. Yang and J. Yao, “Multilayer neurocontrol of high-order uncertain nonlinear systems with active disturbance rejection,” *Int. J. Robust Nonlinear Control*, vol. 34, no. 4, pp. 2972–2987, 2024.
[38] M. Morari, “Robust process control,” *Chem. Eng. Res. Des.*, vol. 65, no. 6, pp. 462–479, 1987.
[39] A. Hyafil, A.-L. Giraud, L. Fontolan, and B. Gutkin, “Neural cross-frequency coupling: connecting architectures, mechanisms, and functions,” *Trends Neurosci.*, vol. 38, no. 11, pp. 725–740, 2015.
[40] A. Bragin, G. Jandó, Z. Nádasdy, J. Hetke, K. Wise, and G. Buzsáki, “Gamma (40–100 hz) oscillation in the hippocampus of the behaving rat,” *J. Neurosci.*, vol. 15, no. 1, pp. 47–60, 1995.
[41] R. T. Canolty, E. Edwards, S. S. Dalal, M. Soltani, S. S. Nagarajan, H. E. Kirsch, M. S. Berger, N. M. Barbaro, and R. T. Knight, “High gamma power is phase-locked to theta oscillations in human neocortex,” *Science*, vol. 313, no. 5793, pp. 1626–1628, 2006.
[42] X. Zhang, W. Zhong, J. Brankačk, S. W. Weyer, U. C. Müller, A. B. Tort, and A. Draguhn, “Impaired theta-gamma coupling in app-deficient mice,” *Sci. Rep.*, vol. 6, no. 1, pp. 1–10, 2016.
[43] H. Pishro-Nik, *Introduction to Probability, Statistics, and Random Processes*, Blue Bell, PA, USA: Kappa Research, LLC, 2014.
[44] M. Stefanovic and M. Safonov, “Safe switching adaptive control: Theory,” *Safe Adaptive Control: Data-Driven Stability Analysis and Robust Synthesis*, Heidelberg, Germany: Springer, pp. 15–40, 2011.